



**HAL**  
open science

## NaYF<sub>4</sub> Microstructure, beyond Their Well-Shaped Morphology

Godefroy Leménager, Sandrine Tusseau-Nenez, Maud Thiriet, Pierre-Eugène Coulon, Khalid Lahlil, Eric Larquet, Thierry Gacoin

► **To cite this version:**

Godefroy Leménager, Sandrine Tusseau-Nenez, Maud Thiriet, Pierre-Eugène Coulon, Khalid Lahlil, et al.. NaYF<sub>4</sub> Microstructure, beyond Their Well-Shaped Morphology. *Nanomaterials*, 2019, 9 (11), pp.1560. 10.3390/nano9111560 . hal-02345184

**HAL Id: hal-02345184**

**<https://hal.science/hal-02345184>**

Submitted on 7 Dec 2020

**HAL** is a multi-disciplinary open access archive for the deposit and dissemination of scientific research documents, whether they are published or not. The documents may come from teaching and research institutions in France or abroad, or from public or private research centers.

L'archive ouverte pluridisciplinaire **HAL**, est destinée au dépôt et à la diffusion de documents scientifiques de niveau recherche, publiés ou non, émanant des établissements d'enseignement et de recherche français ou étrangers, des laboratoires publics ou privés.

Article

# NaYF<sub>4</sub> microstructure, beyond their well-shaped morphology

Godefroy Leménager<sup>1</sup> , Sandrine Tusseau-Nenez<sup>1</sup>, Maud Thiriet<sup>1</sup>, Pierre-Eugène Coulon<sup>2</sup>, Khalid Lahlil<sup>1</sup>, Eric Larquet<sup>1</sup>, Thierry Gacoin<sup>1</sup> 

<sup>1</sup> Laboratoire de Physique de la Matière Condensée,

École Polytechnique, CNRS, Université Paris Saclay, 91128 Palaiseau, France

<sup>2</sup> Laboratoire des Solides Irradiés,

École Polytechnique, CNRS, Université Paris Saclay, 91128 Palaiseau, France.

\* Correspondence: godefroy.lemenager@polytechnique.edu, thierry.gacoin@polytechnique.edu

Version August 18, 2019 submitted to Nanomaterials

**Abstract:** Lanthanide doped nanoparticles are widely investigated for their optical properties. However, the sensitivity of the lanthanide ions to the local symmetry, useful when investigating structural environments, becomes a drawback for optimized properties in the case of poorly controlled crystallinity. In this paper, we focus on  $\beta$ -NaYF<sub>4</sub> nanorods in order to provide a detailed description of their chemical composition and microstructure. The combination of detailed XRD analysis and TEM observations show that strong variation may be observed from particles from a same batch of synthesis, but also when considering small variations of synthesis conditions. Moreover, also the nanorods observed by SEM exhibit a very nice faceted shape, they are far from being monocrystalline and present significant local deviation of crystalline symmetry and orientation. All these structural considerations, sensitively probed by polarized emission analysis, are crucial to be analyzed for the development of optimal systems toward the targeted applications.

**Keywords:** X-ray diffraction; crystalline structure; polarized luminescence

## 1. Introduction

The lanthanide doped NaYF<sub>4</sub> nanoparticles (NPs) are a unique class of luminescent nanoparticles that focus increasing attention due to their efficient up-conversion properties and the ability, through colloid chemistry, to nicely play on a variety of shapes[1–3], length[4,5], doping[6]. In the last decade, these particles have been considered for a large variety of innovative applications such as biological labeling, nanothermometers[7,8], rheometry[9], anti-counterfeiting [10,11].

As in all rare-earth doped luminescent compounds, optical properties (emission efficiency, spectral shapes) are known to result from the intrinsic properties of sensitizing ions modulated by their environment within the host matrix. The effect on spectral shape is of primary importance when d orbitals are involved (Eu<sup>2+</sup>, Ce<sup>3+</sup>), but remains significant for transitions implying only f-electron states. This is well documented in the case of Eu<sup>3+</sup> doped compounds, this ion being considered as a very good probe of local environment, providing good indications on site symmetry through the hypersensitive <sup>5</sup>D<sub>0</sub> – <sup>7</sup>F<sub>2</sub> transition[12]. Much less is known and understood on structure/property relationships in the case of up-conversion compounds, which involve more complex emission scheme and energy levels [12]. NaYF<sub>4</sub>, which is the emblematic compound for up-conversion, is known to exist in two different polymorphs: cubic  $\alpha$ -NaYF<sub>4</sub> and hexagonal  $\beta$ -NaYF<sub>4</sub>. The impact of the host crystal on optical properties is directly evidenced by the poor emission properties of the  $\alpha$ -NaYF<sub>4</sub> as compared to the  $\beta$ -NaYF<sub>4</sub> [ref]. As revealed by a literature survey, the exact structure of the hexagonal  $\beta$ -NaYF<sub>4</sub> phase is not so clear [13–17] since three slightly different crystalline structures (see table 2)

32 have been reported, with small but significant variations of their cell parameters and structures, but  
33 also different host site symmetries.

34 Following our recent study on  $\text{LaPO}_4:\text{Eu}$  nanorods[18], the initial purpose of the present work  
35 was to investigate structure/property relationship in the case of  $\text{NaYF}_4:\text{Yb-Er}$  nanoparticles, with  
36 the objective of understanding and optimizing emission properties including emission yield, spectral  
37 shape of the emission lines and polarization properties. On this way, polarization characterization  
38 rapidly provided evidences that such an investigation would be first limited by the fact that  $\text{NaYF}_4$   
39 nanorods are apparently not monocrystalline and present a significant microstructure. We found that  
40 structural investigations of  $\text{NaYF}_4$  nanoparticles have never been discussed in details despite the  
41 numerous works done on this kind of particles, all obtained following similar routes. We attribute  
42 this lack of interest to the very nice shape of the particles as revealed by SEM pictures, which suggest  
43 an excellent quality of their structure thus hiding interest for such studies. Moreover, polarization  
44 of the emission is not so commonly characterized, and appears to be a very sensitive probe of the  
45 microstructure[18]. All these points motivated the present study, aiming in providing new insights on  
46 the particles microstructure in order to understand and optimize optical properties that are the basis of  
47 increasing number of very exciting applications [19–22].

## 48 2. Experimental section

### 49 2.1. Typical synthesis of the $\text{Er}^{3+}/\text{Yb}^{3+}/\text{Gd}^{3+}$ - $\text{NaYF}_4$ nanorods

50  $\text{GdCl}_3 \cdot 6\text{H}_2\text{O}$  (99.99%),  $\text{YCl}_3 \cdot 6\text{H}_2\text{O}$  (99.99%),  $\text{YbCl}_3 \cdot 6\text{H}_2\text{O}$  (99.99%),  $\text{ErCl}_3 \cdot 6\text{H}_2\text{O}$  (99.99%),  $\text{NaOH}$   
51 (98%),  $\text{NH}_4\text{F}$  (98%),  $\text{NaF}$  (98%) and oleic acid (90%) were all purchased from Sigma-Aldrich and used  
52 as starting materials without any further purification.

53 Synthesis where adapted from the protocols of [23] and [24], which consists in solvothermal  
54 precipitation of chloride lanthanide salts and  $\text{NH}_4\text{F}$  in a water/ethanol/oleic acid mixture.  
55 Experimental conditions are shown on table 1 for samples labeled NRXX for nanorods sample N°XX.  
56 In a typical experiment (eg sample NR11), 30 mmol (1.2 g) of  $\text{NaOH}$  in 5.6 mL of water were mixed  
57 with 20 mL of ethanol (EtOH) and 20 mL of oleic acid (OA) under stirring. To the resulting mixture  
58 were selectively added 0.75 mmol (228 mg) of  $\text{YCl}_3 \cdot 6\text{H}_2\text{O}$ , 0.27 mmol (104.6 mg) of  $\text{YbCl}_3 \cdot 6\text{H}_2\text{O}$ , 0.03  
59 mmol (11.4 mg) of  $\text{ErCl}_3 \cdot 6\text{H}_2\text{O}$ , 0.45 mmol (167 mg) of  $\text{GdCl}_3 \cdot 6\text{H}_2\text{O}$  and 7.7 mmol (278 mg) of  $\text{NH}_4\text{F}$   
60 dissolved in 12 mL of water. The solution was then transferred into a 75 mL autoclave and heated  
61 at 200 ° C for 2 h under stirring. In some cases, the NPs were heated for a longer time (24h instead  
62 of 2h) to remove the  $\alpha$ - $\text{NaYF}_4$  NPs and also a sealed glass tube has been used to test higher pressure  
63 synthesis. After cooling down to ambient temperature, the resulting nanoparticles were precipitated  
64 by addition of 50 mL of ethanol, collected by centrifugation, washed with water and ethanol several  
65 times. They were finally dried and kept as a powder. For the optical experiments, we manipulate  
66 the nanorods (NRs) as aqueous dispersion to ease the manipulation and observations. In this case,  
67 a functionalization by ligand exchange is needed to ensure the good dispersion in water. About 20  
68 mg of  $\text{NaYF}_4$  @oleic acid NPs are sonicated and centrifuged several times with 2 mL aqueous citrate  
69 solution (0.2 M), washed with EtOH and water to remove remaining oleic acid molecules, finally the  
70 nanorods are well dispersed in water.

### 71 2.2. Confocal microscopy

72 The NPs were analyzed by a confocal microscopy system from Nikon (Nikon Eclipse Ti with  
73 confocal module C2 Si). A nanomolar solution of citrate functionalized NPs in water is first sonicated 4  
74 times 45s (450W Branson) to ensure the perfect dispersion of the NRs and then drop-casted on a glass  
75 coverslip. A Tsunami Ti-Sapphire pulsed laser was focused on the NPs with a 60x oil objective. The  
76 polarized resolved spectroscopy was performed by means of a spectrometer (IsoPlane SCT320 from  
77 Princeton Instrument) coupled to CCD (Pixis-400-BX) and a motorized polarizer.

Sample Name	Ln amount			Solvent volume			Heating		Type of content
	Er	Yb	Gd	H <sub>2</sub> O	EtOH	OA	Time	Temp	
NR00	2	18	30	17	20	20	2H	200° C	Autoclave
NR01	2	18	0	17	20	20	2H	200° C	Autoclave
NR02	2	18	0	17	20	20	2H	200° C	Autoclave
NR03	2	18	5	17	20	20	2H	200° C	Autoclave
NR04	2	18	5	17	20	20	20H	200° C	Autoclave
NR05	2	18	15	120	110	110	2H	200° C	Glass tube
NR06	2	18	15	45	50	50	2H	200° C	Glass tube
NR07	2	18	15	45	50	50	20H	200° C	Glass tube
NR08	2	18	30	45	50	50	2H	200° C	Glass tube
NR09	2	18	30	45	50	50	2H30	200° C	Glass tube
NR10	2	18	30	120	110	110	3H	200° C	Autoclave
NR11	2	18	30	17	20	20	2H	200° C	Autoclave
NR12	2	18	45	45	50	50	2H	200° C	Glass tube
NR13	2	18	60	45	50	50	2H	200° C	Glass tube

**Table 1.** Summary of all the synthesis parameters

### 78 2.3. TEM observation

79 Transmission Electron Microscopy (TEM) experiments were performed using a field emission gun  
80 JEOL JEM-2010F microscope operating at 200 kV with a high-resolution HR polar piece ( $C_s = 1.0$  mm,  
81  $C_c = 1.4$  mm, point resolution = 0.24 nm, with a dose of  $\approx 20$  electrons  $\text{\AA}$  at 50,000 magnification and  $\approx$   
82 100 electrons  $\text{\AA}$  at 250,000 magnification). Chemical mapping was performed by XEDS (Cliff-Lorimer  
83 methods) using a FEI Titan Themis probe-corrected microscope operating at 200kV and equipped with  
84 a Scanning Transmission Electron Microscopy (STEM) module at 115,000 and 225,000 magnification  
85 (probe size 1  $\text{\AA}$ ) and "Super-X" detectors (beam convergence angle : 24.6 mrad).

86 During the ions quantification, an amorphization of the NPs may be observed. The loss of the  
87 crystalline structure can increase the ion mobility and change the doping repartition in the NP but not  
88 the average doping of a NP. For this reason, we present only global measurements on whole NPs.

### 89 2.4. X-Ray diffraction: ESRF

90 The synchrotron X-Ray powder diffraction experiments were carried out at the Swiss-Norwegian  
91 Beam-Lines (BM1A station) of the European Synchrotron Radiation Facility (ESRF), France. A  
92 monochromatic beam of wavelength  $\lambda = 0.7129$   $\text{\AA}$  was focused onto the sample by sagittal bending of  
93 the second crystal of a double-crystal Si(111) monochromator using additional slits of  $272.26 * 327.34$   
94  $\mu\text{m}^2$ . X-Ray Powder Diffraction (XRPD) data were collected in transmission geometry using a  
95 pixel-array detector (PILATUS 2M, Dectris Ltd). Samples were sealed in 0.4 mm diameter glass  
96 capillaries and rocked by  $10^\circ$  during data collection. The instrumental resolution was determined  
97 using a LaB<sub>6</sub> NIST standard (Standard Reference Material 660a, cell parameter =  $0.41569162$  nm  $\pm$   
98  $0.00000097$  nm at  $22.5^\circ\text{C}$ ).

99 The selected patterns for the identification of phases by XRPD and the crystallographic data (COD  
100 database [25]) for the line profile analysis are summarized in Table 2.

## 101 3. Results and discussion

### 102 3.1. Confocal microscopy and polarized luminescence

103 With our confocal set-up, the polarized spectra of our NPs deposited by drop-casting of diluted  
104 NaYF<sub>4</sub> NPs in water are measured. The low concentration coupled to a sonication of the solution just  
105 prior deposition leads to dispersed NPs on the glass coverslip. Without reference, the orientation of the  
106 NP cannot be known nor the expected orientation of the polarization. We measured the spectra for a

Phase	Space group	Cell parameters (Å)	Atomic positions	Occupancy	Re site symmetry	COD ID	ref
Hexagonal ( $\beta$ )	$P6_3/m$ 176	$a = b =$ 5.99276 $c =$ 3.52281	Y $2/3$ $1/3$ $1/4$ Na $2/3$ $1/3$ $1/4$ Na $0$ $0$ $z$ F $x$ $y$ $1/4$	0.75 0.25 0.25 0.25	$C_{3h}^2$	1517675	[26]
Hexagonal ( $\beta$ )	$P\bar{6}$ 174	$a = b =$ 5.99276 $c =$ 3.52281	Y $2/3$ $1/3$ $1/2$ Y $0$ $0$ $0$ Na $2/3$ $1/3$ $1/2$ Na $1/3$ $2/3$ $z$ F $x$ $y$ $1/2$ F $x$ $y$ $0$	0.5 0.75 0.5 0.5 1 1	$C_{3h}^2$ $C_{3h}^2$	1517672	[26]
Hexagonal ( $\beta$ )	$P\bar{6}2m$ 189	$a = b =$ 5.9148 $c =$ 3.52281	Y $1/3$ $2/3$ $1/2$ Y $0$ $0$ $0$ Na $1/3$ $2/3$ $1/2$ F $x$ $0$ $0$ F $0$ $1/2$	0.25 1 0.75 1 1	$C_{3h}^1$ $C_3^1$	1517674	[26]
cubic ( $\alpha$ )	$FM\bar{3}m$ 225	$a = b = c =$ 5.47000	Y $0$ $0$ $0$ Na $0$ $0$ $0$ F $1/4$ $1/4$ $1/4$	0.5 0.5 1	$O_h$	1517676	[27]

**Table 2.** Crystallographic data on synthesized phases of  $NaYF_4$  for phase identification and rare-earth (Re) ion site symmetry

107 wide range of polarization angle. In these conditions, the axes of the two orthogonal electric dipoles will  
 108 be given by the least brilliant and the brightest spectra. In Fig. 1.a we present the photoluminescence  
 109 (PL) spectrum for two orthogonal polarizations (red and blue) and the difference between them in  
 110 green. Moreover, by plotting the PL intensity versus the polarization angle (see Fig. 1.b), the typical  
 111 dipole-like behavior expected from lanthanide ions appears to be in good approximation with the  
 112 Malus law.

113 However, if we look in detail this dependence for several wavelengths, the extreme values are  
 114 not obtained for the same angles as expected. Indeed, the polarization is due to the site symmetry  
 115 of the lanthanide ion and the electrons can optically relax by emitting  $\alpha$ ,  $\sigma$  or  $\pi$  photons [28] with  
 116 orthogonal polarization. Then a PL dependence can only present two angles for the PL optima values  
 117 for all measured transitions, which is not the case: the 665.0 nm transition has a maximum shifted  
 118 of  $20^\circ$  as compared to another transitions at 662.9 nm. This observation leads to conclude that the  
 119 local symmetry orientation is not the same for all the emitters. To understand this observation, we  
 120 investigated the microstructure of the particles in more details.

### 121 3.2. TEM observation and doping homogeneity

122 The doping of the  $NaYF_4$  NPs (nature and concentration of the rare earth ions) plays an  
 123 unquestionable part in the shape and structure of the NPs[3]. Several batches of NPs were synthesized  
 124 with different nominal doping concentrations. The effective doping of NPs was measured by EDX  
 125 analysis. The table 3 presents the expected and effective doping of particles obtained from different  
 126 syntheses and shown in figure 2.

127 The three first samples were prepared under similar conditions (doping concentration, heating  
 128 temperature and time). However, the effective dopings are found to be different: NRs are less rich in  
 129 Y of about 20 mol%, more than 3 times more rich in Er whereas Yb and, in a minor way, Gd doping  
 130 are close to the expected values. This shows the sensitivity of the synthesis to some parameters that  
 131 can be associated to the volume of solvent and the type of container, that could affect for example the  
 132 pressure during the synthesis.

133 TEM observations evidences two situations. On one hand, we sometime observe in the same  
 134 batch two (or more) populations of NPs, each one having a relatively low size dispersion. However,

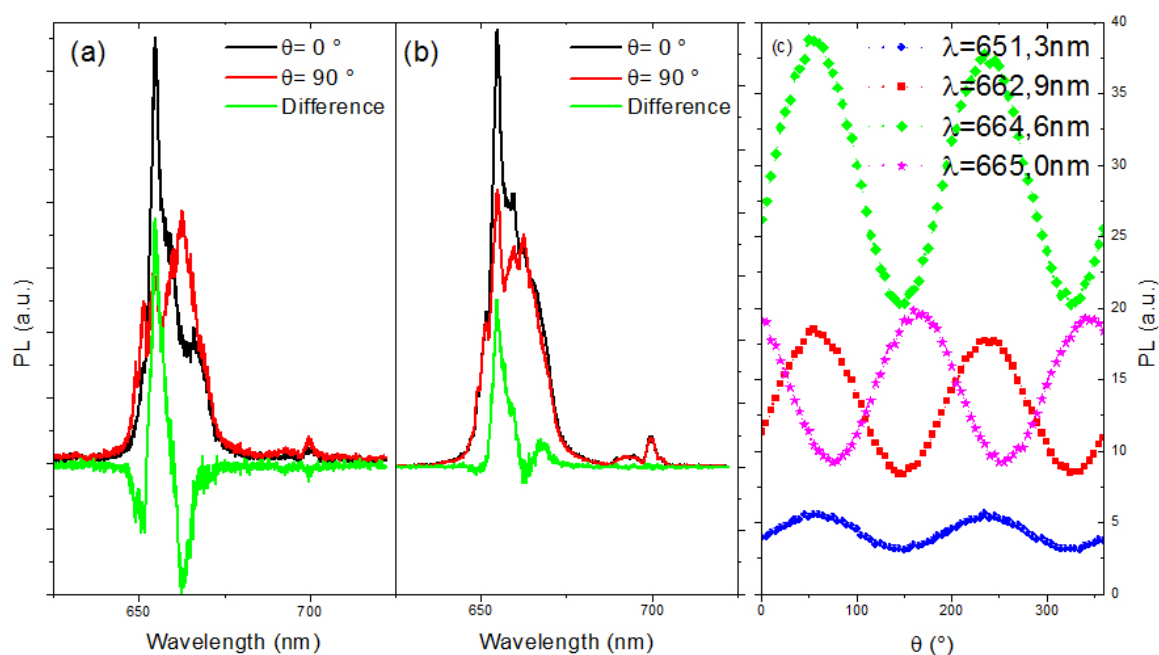


**Figure 1.** (a-b) Spectrum for two orthogonal polarizations (red and black) and the difference between them (green) for two different NPs of the same batch NR07. (c) PL intensity versus polarization for different wavelengths.

Sample name	TEM size (nm)		Aspect Ratio	Expected doping (mol%)				Measured doping (mol%)				Area in Fig. 2
	L	D		Y	Er	Yb	Gd	Y	Er	Yb	Gd	
NR00	300	50	6	50	2	18	30	40.2	9.4	18.2	32	
NR09	150	60	2.5	50	2	18	30	40.0	6.9	15.6	38.6	
NR11	200	30	6.6	50	2	18	30	41.5	8.4	17.5	32	1
	640	100	6.4					56	6.7	13.4	18	2
NR13	55	40	1.4	20	2	18	60	13.3	14.5	13.5	58	4
	130	35	3.7					23.9	14.6	13.9	47.6	3

**Table 3.** Expected and effective doping concentration of different NPs measured by EDX. Two lines in the tabular correspond to two population measured by EDX. The NPs sizes given come from the measured NPs and can differ from the mean values.

135 the size of each population can be very different as it is illustrated in Fig. 2 for two syntheses (NR11  
 136 and NR13). The EDX measurements of the delimited area give us the chemical composition as reported  
 137 in the table 3. For each population, we measure a strong difference in the gadolinium concentration  
 138 (and in consequence the yttrium concentration) while erbium and ytterbium concentrations present  
 139 only small variations. In Fig. 2.a, the NP in the area (1) delimited by the dotted green line area has a  
 140 concentration of gadolinium of 32 mol% and its size is typical from this synthesis (50 \* 260 nm), while  
 141 the NP shown by the continuous red line (area 2) has a concentration of only 18 mol% and its size is  
 142 twice the average size (110 \* 650 nm) with a similar aspect ratio. Another example for the batch NR013  
 143 is presented in Fig. 2.b where the same behavior is observed with a complete different aspect ratio.  
 144 While the experimental conditions are exactly the same, one (NR00) or two populations of particle  
 145 sizes (NR11) are observed, with identical aspect ratios (about 6). At this stage, no clear parameter can  
 146 explain these results but this is probably an evidence that the two kind of particles formed at different  
 147 time during the synthesis, probably because the kinetic of formation of Gd rich or Gd poor particles is  
 148 different.

149 On the other hand, the expected doping and the effective doping can differ strongly. Depending  
 150 on the synthesis, the gadolinium concentration expected to be around 30%, is found to vary from

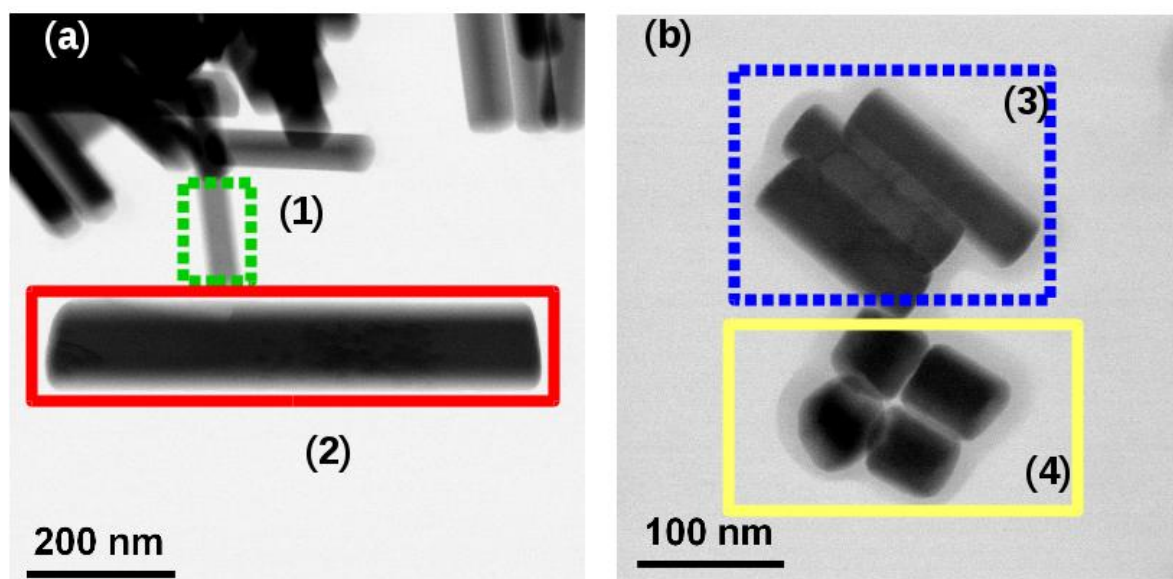


**Figure 2.** Two TEM images of NaYF<sub>4</sub> NPs from the two batches presenting two NPs populations ((a) NR11 and (b) NR13)

151 18% to 38%. Two samples share a population with the same doping while the first sample presents  
 152 a different doping. The two last experiments were done with another solvent ratio compared to the  
 153 first experiment resulting in a different pressure during the synthesis. These differences in pressure,  
 154 solvent composition and the correlated solubility can explain the doping difference between the first  
 155 and the two last syntheses.

### 156 3.3. Phase identification and doping dependence

157 In Fig. 3.b, we present one typical diffraction pattern obtained for a mixture of  $\alpha$ -NaYF<sub>4</sub> and  
 158  $\beta$ -NaYF<sub>4</sub> phases. The mixture of these two types of structure can easily be studied independently  
 159 since they exhibit clearly different diffraction patterns. Not all of our syntheses result in a mixture  
 160 of  $\alpha$ -NaYF<sub>4</sub> and  $\beta$ -NaYF<sub>4</sub> nanoparticles - we focused our work on  $\beta$ -NaYF<sub>4</sub> nanorods as this phase  
 161 provides the interesting optical properties. As previously mentioned, the  $\beta$ -NaYF<sub>4</sub> NPs can adopt three  
 162 different crystalline structures, with space groups depending on the synthesis parameters known to be  
 163 P6<sub>3</sub>/m, P $\bar{6}$  and P $\bar{6}2$ m (see Fig. 3) [26]. The main difference between the powder diffraction patterns  
 164 lies in an extra peak from the (001) planes for the P $\bar{6}$  and P $\bar{6}2$ m compared with the P6<sub>3</sub>/m patterns at  
 165  $2\theta = 11.70^\circ$  in our experimental conditions. The intensity of this peak is very low, estimated around 2%  
 166 of the maximum diffraction peak intensity and below 0.1% respectively for P $\bar{6}$  and P $\bar{6}2$ m. This small  
 167 difference is usually not visible in XRPD done with a usual laboratory diffractometer and was at the  
 168 origin of long discussions in the literature [13,14]. The P $\bar{6}$  and P-62m can only be distinguished by a  
 169 quantitative analysis of the peak intensities. A synchrotron facility is required to properly determine  
 170 the symmetry of NaYF<sub>4</sub> NPs.

171 For the  $\beta$ -NaYF<sub>4</sub> NRs, among the thirteen studied samples, only one of them presents a detectable  
 172 specific peak of the P $\bar{6}$  or P $\bar{6}2$ m structure. Furthermore, the intensity of this peak is very low (0.1%  
 173 of the maximum intensity) indicating that only a negligible portion or region of the particles was obtained  
 174 with this structure. For these reasons, only the P6<sub>3</sub>/m structure was considered in the following for  
 175 our NPs.

176 After the phase identification, the Fullprof software [29,30] was used in profile matching mode  
 177 with a constant scale factor in order to perform a microstructural analysis. The XRPD patterns were  
 178 fitted with a Thompson-Cox-Hastings function [31] (a modified pseudo-Voigt function) to extract, for  
 179 each phase ( $\alpha$  and/or  $\beta$ -NaYF<sub>4</sub>), the cell parameters and the width and breadth (full width at half

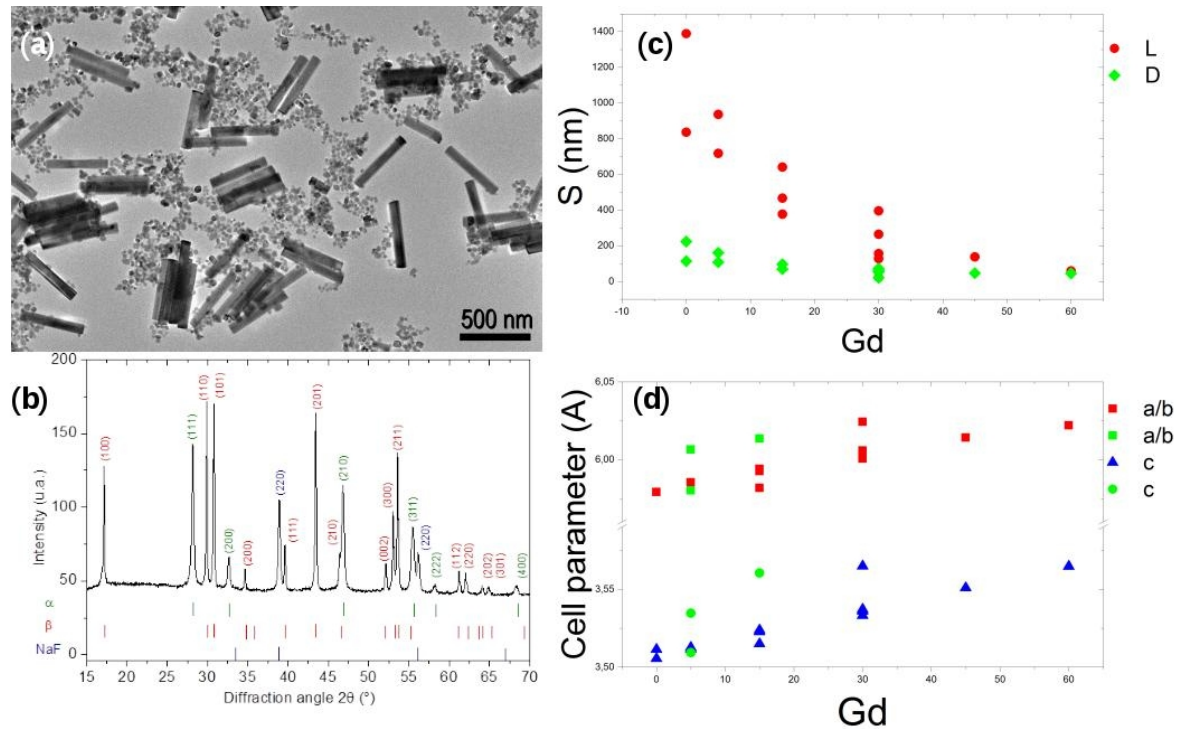


**Figure 3.**  $\text{NaYF}_4$  nanoparticles (a) TEM image with small cubes ( $\alpha\text{-NaYF}_4$ ) big nanorods ( $\beta\text{-NaYF}_4$ ) (b) typical X-Ray pattern of these particles (c) TEM NPs sizes  $S$  ( $L$  = length,  $D$  = diameter) and (d) cell parameter dependences vs Gd nominal doping with blue triangles and red squares for the main set of cell parameters of each batch and green stars and green circles for the second set of cell parameters

180 maximum FWHM and integral breadth  $IB$ ) of the Bragg peaks. Our study focuses on profile fitting  
 181 and diffraction line broadening analysis. As said previously, the particles are doped with a constant  
 182 nominal concentration of ytterbium (18 mol %) and erbium (2%) and we only changed the gadolinium  
 183 concentration (from 0% to 60%). On the contrary to EDX focusing on single or few NPs, XRPD gives a  
 184 global and averaged analysis of the sample.

185 Fig. 3.d presents the evolution of the cell parameters with the nominal gadolinium content of the  
 186  $\beta\text{-NaYF}_4$  phase. In some samples (NR03, NR 04 and NR06), two  $\beta\text{-NaYF}_4$  phases are identified, a main  
 187 peak is observed at the expected position and a second one slightly shifted (shoulder or separated  
 188 peak, associated to other set of cell parameters shown in Fig. 3.d with a green star or circle). It is not  
 189 possible to associate the two phases observed here with the two populations previously observed with  
 190 the EDX. However, the two results are similar and result reinforce themselves. Moreover, both sets  
 191 present in parallel a linear dependence with the amount of gadolinium (even with the poor statistic  
 192 of the second group). The second set of cell parameters cannot be explained by a population with a  
 193 higher gadolinium concentration as observed previously. Yet, the linear dependency is expected due  
 194 to the higher ionic radius of the gadolinium compared to yttrium.

### 195 3.4. Microstructural analysis

196 For all the 13 studied samples, all XRPD patterns exhibit peaks broader than the instrumental  
 197 resolution (typically the FWHM for the samples was above  $0.050^\circ 2\theta$  to be compared with  $0.029^\circ 2\theta$   
 198 for the  $\text{LaB}_6$  standard pattern). This broadening is known to be due to size effect and/or microstrain  
 199 in the system. From our previous fit, the shape factors ( $\phi$ ) can be defined by  $\phi = IB_{v0}/FWHM_{v0}$   
 200 with  $IB_{v0}$  the observed integral breath (IB) and the observed Full Width at Half-Maximum (FWHM).  
 201 The Lorentzian and Gaussian limits for the shape factors are respectively  $\phi = 2/\pi \approx 0.6366$  and  
 202  $\phi = 2(\frac{\log_e(2)}{\pi})^{1/2} \approx 0.93949$  [32]. Shape factor with  $\phi < 0.6366$  and  $\phi > 0.9394$  can be referred as super

203 Lorentzian and super Gaussian respectively [32]. Otherwise, it implies that the profile is a convolution  
 204 of both shapes and justifies the use of a pseudo-Voigt.

205 It is well admitted now that, for small geometrical effects of a single line instrument, the  
 206 instrumental profile is approximately Lorentzian, whereas the profile arising from lattice strain is more  
 207 Gaussian [33,34]. The broadening due to defaults or small crystallite size depends respectively on  
 208 their nature of the shape and the size distribution of the crystallites, and is assumed to be Lorentzian.  
 209 These components can be taken as Voigtian, the Lorentzian and Gaussian parts are the limiting cases.  
 210 If two or more reflections are available, size and strain effects can be determined from the variation of  
 211 Lorentzian and Gaussian contributions in the IB depending on the hkl Miller indices [35].

212 We followed the procedure recommended by Langford [32], computing the FWHM and IB of a  
 213 pseudo-Voigt profile from the broadened profile to give the shape factor, calculating the breadths of  
 214 the constituent profiles corrected by the instrumental broadening and analyzing the Williamson-Hall  
 215 [36] and Halder-Wagner [37,38] plots. The empirical procedure derived by de Keijser *et al.*[35] for  
 216 calculating the Lorentzian and Gaussian components ( $\beta_L$ ,  $\beta_G$ ) and the integral breadth (IB) has  
 217 been used in the Fullprof software.

218 The figure 4.a presents the dependence of the shape factor for four typical samples (NR 04-07-09-10)  
 219 and the most different one (NR13), all the peaks show a shape factor between Gaussian and Lorentzian  
 220 limits. The shape factor may not correlated with the Gd concentration (Fig 4.b) To understand  
 221 the origin of the broadening of our peaks, possibly due to both size and microstrain contribution,  
 222 the Halder-Wagner method [37,38] is recommended with such profile parameters instead of a  
 223 Williamson-Hall approach [36], as the peaks have not a pure Lorentzian shape. Note that the fit  
 224 is not so dependent on the  $2\theta$  range, even if Halder-Wagner plot insists on the small  $2\theta$  values (however  
 225 the most intense peaks).

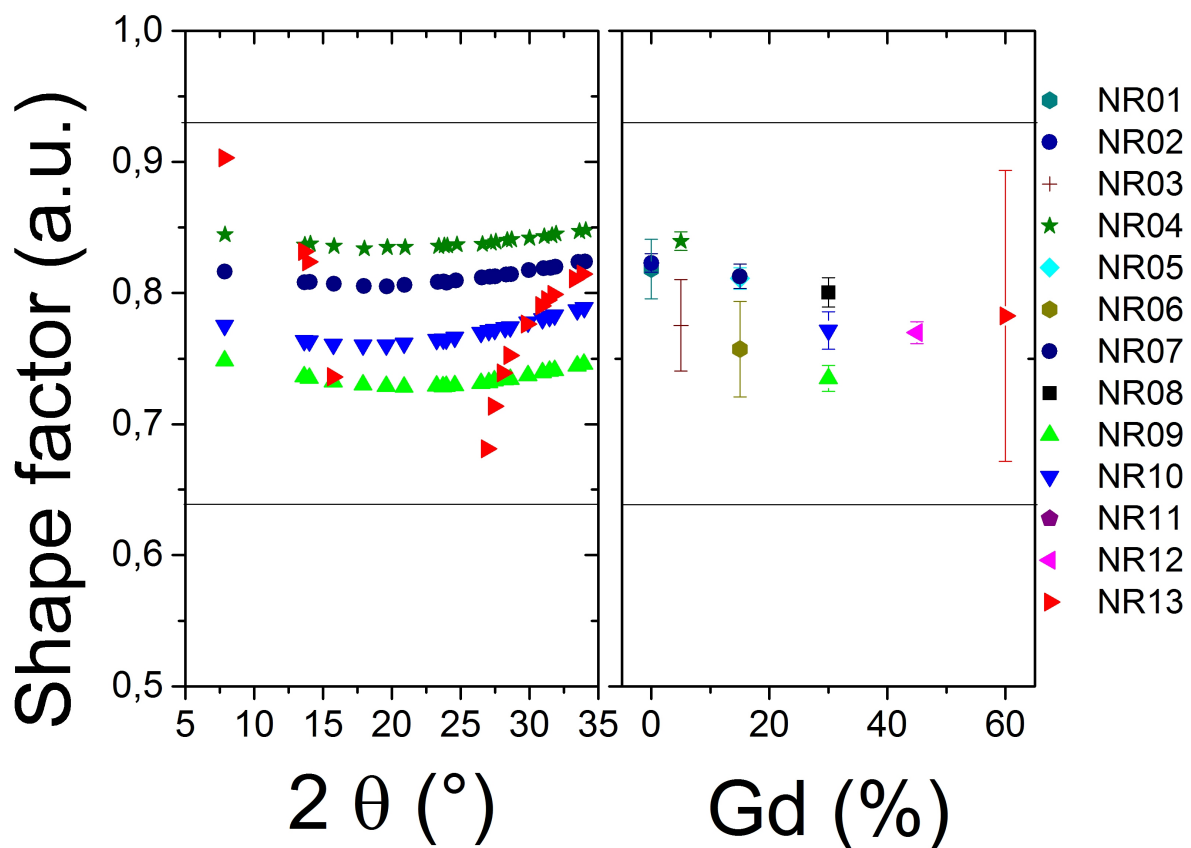


**Figure 4.** (a) Shape factor for each peak of four typical samples (NR04, NR07, NR09, NR10) and the most different sample (NR13) (b) Mean shape factor versus the expected gadolinium concentration

	TEM size (nm)		AR	Gd (mole %)	$y = ax + b$		shape factor	Crystallite size (nm)	microstrain
	L	D			a	b			
NR01	835	113	7.4	0	1.16	1.69	0.89	85	2.5e-4
NR02	1390	234	5.9	0	0.92	0.42	0.82	108	1.3e-4
NR03	718	108	6.6	5	1.35	0.29	0.77	74	1e-4
NR04	935	160	5.8	5	0.98	0.46	0.83	102	1.35e-4
NR05	375	70	5.4	15	1.69	0.79	0.81	59	1.7e-4
NR06	465	70	6.6	15	1.44	2.9	0.76	69	3.4e-4
NR07	640	100	6.4	15	1.3	0.8	0.81	77	1.8e-4
NR08	400	55	7.2	30	2.01	0.36	0.8	50	1.2e-4
NR09	156	62	2.5	30	2.01	-0.21	0.73	50	n.s.
NR10	130	70	1.9	30	2.04	0.53	0.77	49	1.5e-4
NR11	260	55	4.7	30	2.21	1.08	0.80	45	2e-4
NR12	137	45	3	45	2.83	0.72	0.77	35	1.7e-4
NR13	60	45	1.3	60	3.9	-6	0.78	26	n.s.

**Table 4.** Main parameters of the studied NPs (with L for Length, D for Diameter, AR for Aspect Ratio) and the parameters from the Halder-Wagner graph with the apparent size and microstrain obtained for each of them. Here only the expected gadolinium concentration is given. (n.s. negative microstrain even if the value is very close to zero)

226 To distinguish between size and microstrain respective contributions, the Halder-Wagner equation  
 227 is written as  $(b^*/d^*)^2 = IB^*/(d^*)^2$ . By plotting this equation a linear behavior is observed for all  
 228 our samples (Fig. 5). The intercept of the linear regression in the Halder-Wagner plot is related to  
 229 the importance of microstrain in the material and, on the other hand, the slope is related to a mean  
 230 apparent size (in volume) of the NPs.

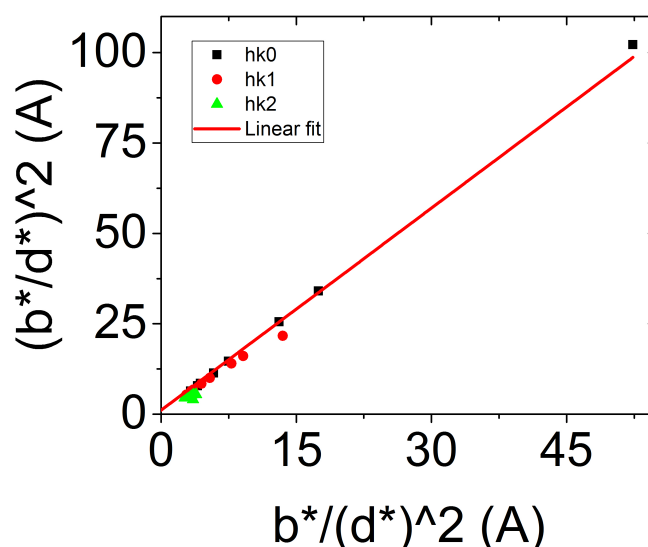


**Figure 5.** Halder-Wagner plot for a typical sample

231 In Fig. 5, here for NR08, a clear linear regression is observed, with an origin close to zero. This  
 232 behavior is common to all our synthesized NPs, as summarized in table 4. Whatever the sample the  
 233 microstrains are close to zero. For the rest of the study, the broadening of the Bragg peaks is then  
 234 considered to be the broadening of a size effect only, and the microstrain effect can be neglected. One  
 235 can also notice that the characteristic size of the NPs obtained from the Halder-Wagner plot is smaller  
 236 than the one obtained by TEM imaging. In first approximation, it appears that the size obtained by  
 237 XRD is close to the diameter of the NPs observed by TEM. This lead us to study more carefully the  
 238 crystallinity of our NPs to understand the meaning of this characteristic size.

	TEM size (nm)		AR	Gd (mol%)	Crystallite size (nm)	
	L	D			min	max
NR01	835	113	7.4	0	77	100
NR02	1390	234	5.9	0	143	153
NR03	718	108	6.6	5	79	180
NR04	935	160	5.8	5	132	142
NR05	375	70	5.4	15	65	77
NR06	465	70	6.6	15	63	69
NR07	640	100	6.4	15	89	93
NR08	400	55	7.2	30	58	102
NR09	156	62	2.5	30	52	110
NR10	130	70	1.9	30	57	74
NR11	260	55	4.7	30	51	87
NR12	137	45	3	45	40	92
NR13	60	45	1.3	60	36	36

**Table 5.** Main parameters of the studied NPs (with L for Length, D for Diameter, AR for Aspect Ratio) and the apparent size obtained by the anisotropic model. Here only the nominal gadolinium concentration is given.

The previous observation was assuming an isotropic NPs shape, supposed to be spherical. Now a Scherrer-type analysis was used, where only the Lorentzian contribution is considered for each individual reflection in order to take into account eventual anisotropic broadening, to obtain the size of the crystallite, a needle-like model was applied - with a main axis along the c axis or [001] direction. Remember that by this method it is at best a mean value of the size of the coherent domains of a supposedly unimodal distribution of crystallites which is obtained for each (hkl) Bragg peak.

From this analysis, the three dimensions of the crystallites in our NPs can be extracted. All of them present a longer length along the [001] direction and a smaller size in the corresponding orthogonal [hk0] directions. Moreover, in most cases, the length along this direction [hk0] is slightly smaller than the apparent size observed by TEM. We summarized the crystallite sizes in the table 5 with again the apparent size for an easier comparison.

As previously said, the smallest length of the crystallites is associated to the directions orthogonal to c-axis. Moreover, for NPs with a diameter below 100 nm, this length is almost always slightly smaller of few nanometers than the diameter of the NPs. This fact was explained with the HRTEM observation. In Fig. 6.a or b, we observed an amorphous phase or a less crystallized shell around the NPs. Another observation, more surprising from our point of view, is the possibility to have a well crystallized phase in an orthogonal direction surrounding the core of the NPs. The inset of Fig. 6.a shows the FFT of the area delimited by the dotted green line. This FFT presents a rectangular signal characteristic from an hexagonal structure seen orthogonally of the c-axis. Even though the NPs in Fig. 6.c is a rod well defined, the FFT of the area delimited by the continuous red line is characteristic from an hexagonal phase through the c-axis. Note that the crystallinity of the NPs presented is not altered by the electron beam of the TEM.

This observation is important if we want to analyze the luminescence of the NPs. It is well known that lanthanide ions have a specific luminescence correlated with their local environment. For a structure like  $P6_3/m$ , the doping ions have access to only one type of site as mentioned in table 2. The luminescence and in particular the polarized properties will be depending of this site (here  $C_{3h}^2$ )[28]. But if the crystallinity of the NPs is not good meaning polycrystallines nanorods instead of monocrystalline and the lanthanide-site are not well aligned with a well-defined c-axis along the whole rod, the optical properties will be affected starting with a reduction of the polarization degree. Moreover, for singles NPs studies, due to statistical variation from one NP to another, it will be difficult to analyze the optical properties.

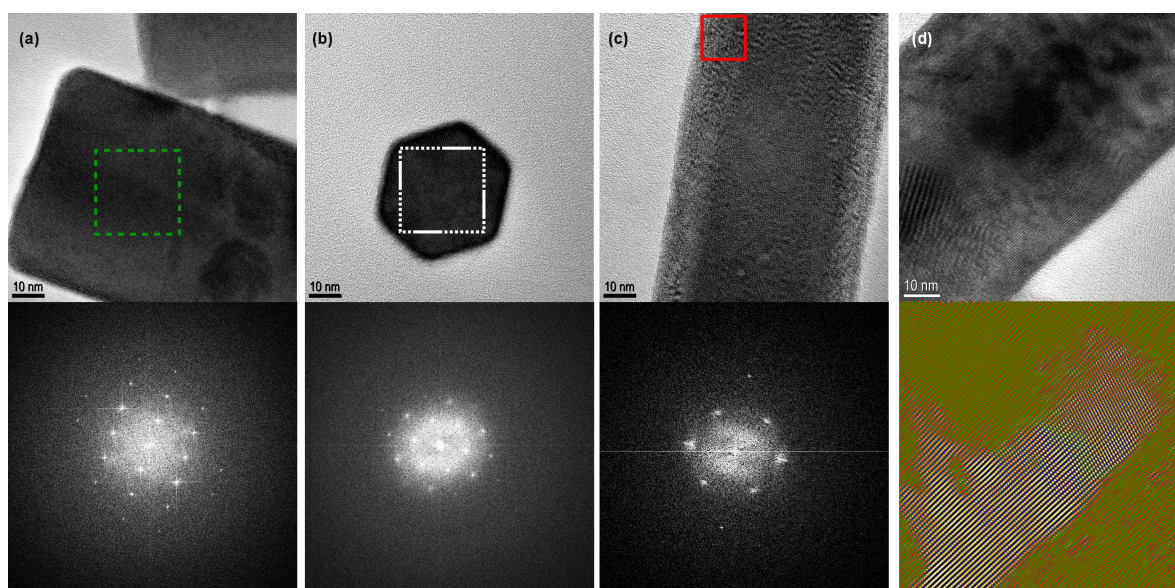


**Figure 6.** (a-c) HRTEM of NPs with below the FFT of the indicate area (a) NR09 with a typical FFT orthogonal to the c-axis (b) NR13 with a typical FFT parallel to the c-axis (c) NR11 with a FFT characteristic from an hexagonal phase trough the c-axis but observed orthogonally to the c-axis. (d) HRTEM of a NR06 with various defects below same image filtered with false color.

#### 270 4. Conclusion

271 Many works have reported the synthesis, optical properties and application of Na(Gd)YF<sub>4</sub>:Yb, Er  
 272 nanoparticles. The large interest for this systems comes both from their highly appealing emission  
 273 properties, and the ability to synthesis particles with different size and shapes. In particular, very nice  
 274 faceted nanorods can be obtained with adjustable aspect ratio playing on the particles composition  
 275 such as some Gd<sup>3+</sup> ions in substitution to Y<sup>3+</sup>. Nevertheless, characterizations of polarized emission  
 276 from single nanorods evidence that the particles are not monocrystals, which motivated this study to  
 277 get a deeper insight in the particles microstructure. This work has been done using TEM and XRD  
 278 analysis on a set of 13 samples obtained under various conditions. We could show that in a given  
 279 batch of synthesis, and focusing on particles with the  $\beta$ -NaYF<sub>4</sub> structure, different populations of  
 280 particles may coexist with different size and shape, but also with strong deviations from the nominal  
 281 composition. XRPD analysis using the Halder-Wagner approach, combined with HRTEM point  
 282 out an anisotropic polycrystalline structure of the nanorods with important local variations of the  
 283 crystallites orientations. This is clearly at the origin of the polarization spectra, which is very sensitive  
 284 to crystallites orientation.

285 As NaYF<sub>4</sub> NPs are now widely used for their interesting optical properties, these observations  
 286 show that an exhaustive structural and chemical analysis is compulsory in the aim to understand and  
 287 optimize this system for the targeted applications.

288 **Author Contributions:** Conceptualization, Godefroy Leménager and Sandrine Tusseau-Nenez; Data curation,  
 289 Godefroy Leménager and Sandrine Tusseau-Nenez; Formal analysis, Godefroy Leménager and Sandrine  
 290 Tusseau-Nenez; Funding acquisition, Thierry Gacoin; Investigation, Godefroy Leménager; Methodology, Godefroy  
 291 Leménager and Sandrine Tusseau-Nenez; Project administration, Godefroy Leménager; Resources, Godefroy  
 292 Leménager, Sandrine Tusseau-Nenez, Maud Thiriet, Pierre-Eugène Coulon, Khalid Lahlil, Eric Larquet and  
 293 Thierry Gacoin; Software, Sandrine Tusseau-Nenez; Supervision, Godefroy Leménager; Validation, Godefroy  
 294 Leménager, Sandrine Tusseau-Nenez and Thierry Gacoin; Visualization, Godefroy Leménager; Writing – original  
 295 draft, Godefroy Leménager and Sandrine Tusseau-Nenez; Writing – review editing, Godefroy Leménager,  
 296 Sandrine Tusseau-Nenez and Thierry Gacoin.

297 **Funding:** Funding for this project was provided by the French National Research Agency in the frame-work of  
 298 the FiPlaNT project (ANR-12-BS10-012).

309 This work was supported by the French ANR research programm "Investissements d'avenir"  
300 (ANR-10-EQPX-50).

301 **Acknowledgments:** We acknowledge the European Synchrotron Radiation Facility for provision of synchrotron  
302 radiation facilities and we would like to thank Adeline Adam, Lucio Martinelli and Isabelle Maurin for the help  
303 during the experiment.

304 **Conflicts of Interest:** The authors declare no conflict of interest.

## 305 References

- 306 1. Li, C.; Quan, Z.; Yang, J.; Yang, P.; Lin, J. Highly Uniform and Monodisperse  $\beta$ -NaYF<sub>4</sub>:Ln<sup>3+</sup> (Ln = Eu, Tb,  
307 Yb/Er, and Yb/Tm) Hexagonal Microprism Crystals Hydrothermal Synthesis and Luminescent Properties.  
308 *Inorganic Chemistry* **2007**, *46*, 6329–6337.
- 309 2. Zhou, J.; Chen, G.; Zhu, Y.; Huo, L.; Mao, W.; Zou, D.; Sun, X.; Wu, E.; Zeng, H.; Zhang, J.; Zhang, L.; Qiu,  
310 J.; Xu, S. Intense multiphoton upconversion of Yb<sup>3+</sup>–Tm<sup>3+</sup> doped  $\beta$ -NaYF<sub>4</sub> individual nanocrystals by  
311 saturation excitation. *Journal of Materials Chemistry C* **2014**, *3*, 364–369.
- 312 3. Liang, X.; Wang, X.; Zhuang, J.; Peng, Q.; Li, Y. Synthesis of NaYF<sub>4</sub> Nanocrystals with Predictable Phase  
313 and Shape. *Advanced Functional Materials* **2007**, *17*, 2757–2765. doi:10.1002/adfm.200600807.
- 314 4. Shi, F.; Zhao, Y. Sub-10 nm and monodisperse  $\beta$ -NaYF<sub>4</sub>:Yb,Tm,Gd nanocrystals with intense ultraviolet  
315 upconversion luminescence. *Journal of Materials Chemistry C* **2014**, *2*, 2198–2203. doi:10.1039/C3TC32303J.
- 316 5. Wang, F.; Han, Y.; Lim, C.S.; Lu, Y.; Wang, J.; Xu, J.; Chen, H.; Zhang, C.; Hong, M.; Liu, X.  
317 Simultaneous phase and size control of upconversion nanocrystals through lanthanide doping. *Nature*  
318 **2010**, *463*, 1061–1065. doi:10.1038/nature08777.
- 319 6. Zhang, Y.; Huang, L.; Liu, X. Unraveling Epitaxial Habits in the NaLnF<sub>4</sub> System for Color  
320 Multiplexing at the Single-Particle Level. *Angewandte Chemie International Edition* **2016**, *55*, 5718–5722.  
321 doi:10.1002/anie.201511626.
- 322 7. Vetrone, F.; Naccache, R.; Zamarrón, A.; Juarranz de la Fuente, A.; Sanz-Rodríguez, F.; Martínez Maestro, L.;  
323 Martín Rodríguez, E.; Jaque, D.; García Solé, J.; Capobianco, J.A. Temperature Sensing Using Fluorescent  
324 Nanothermometers. *ACS Nano* **2010**, *4*, 3254–3258. doi:10.1021/nn100244a.
- 325 8. Brites, C.D.S.; Lima, P.P.; Silva, N.J.O.; Millán, A.; Amaral, V.S.; Palacio, F.; Carlos, L.D. Lanthanide-based  
326 luminescent molecular thermometers **2011**. *35*, 1177–1183. doi:10.1039/C0NJ01010C.
- 327 9. Rodríguez-Sevilla, P.; Zhang, Y.; de Sousa, N.; Marqués, M.I.; Sanz-Rodríguez, F.; Jaque, D.; Liu, X.;  
328 Haro-González, P. Optical Torques on Upconverting Particles for Intracellular Microrheometry. *Nano*  
329 *Letters* **2016**. doi:10.1021/acs.nanolett.6b04583.
- 330 10. Wang, L.; Li, Y. Na(Y<sub>1.5</sub>Na<sub>0.5</sub>)F<sub>6</sub> Single-Crystal Nanorods as Multicolor Luminescent Materials. *Nano*  
331 *Letters* **2006**, *6*. doi:10.1021/nl060684u.
- 332 11. Zhang, Y.; Zhang, L.; Deng, R.; Tian, J.; Zong, Y.; Jin, D.; Liu, X. Multicolor Barcoding in a Single  
333 Upconversion Crystal. *Journal of the American Chemical Society* **2014**, *136*, 4893–4896. doi:10.1021/ja5013646.
- 334 12. Binnemans, K. Interpretation of europium(III) spectra. *Coordination Chemistry Reviews* **2015**, *295*, 1–45.  
335 doi:10.1016/j.ccr.2015.02.015.
- 336 13. Tu, D.; Liu, Y.; Zhu, H.; Li, R.; Liu, L.; Chen, X. Breakdown of Crystallographic Site Symmetry  
337 in Lanthanide-Doped NaYF<sub>4</sub> Crystals. *Angewandte Chemie International Edition* **2013**, *52*, 1128–1133.  
338 doi:10.1002/anie.201208218.
- 339 14. Karbowski, M.; Cichos, J.; Rudowicz, C. Spectroscopic determination of site symmetry and space group in  
340 lanthanide-doped crystals: Resolving intricate symmetry aspects for  $\beta$ -NaLnF<sub>4</sub>. *Polyhedron* **2016**, *105*, 42–48.  
341 doi:10.1016/j.poly.2015.11.044.
- 342 15. Dinic, I.Z.; Mancic, L.T.; Rabanal, M.E.; Yamamoto, K.; Ohara, S.; Tamura, S.; Koji, T.; Costa, A.M.L.M.;  
343 Marinkovic, B.A.; Milosevic, O.B. Compositional and structural dependence of up-converting rare earth  
344 fluorides obtained through EDTA assisted hydro/solvothermal synthesis. *Advanced Powder Technology*  
345 **2016**. doi:10.1016/j.apt.2016.09.021.
- 346 16. Szczyk, B.; Roszak, R.; Roszak, S. Structure of the hexagonal NaYF<sub>4</sub> phase from first-principles molecular  
347 dynamics. *RSC Adv* **2014**, *4*, 22526–22535. doi:10.1039/C4RA00211C.

- 348 17. Hudry, D.; Abeykoon, A.M.M.; Dooryhee, E.; Nykypanchuk, D.; Dickerson, J.H. Probing the Crystal  
349 Structure and Formation Mechanism of Lanthanide-Doped Upconverting Nanocrystals. *Chemistry of*  
350 *Materials* **2016**, *28*, 8752–8763. doi:10.1021/acs.chemmater.6b04140.
- 351 18. Chaudan, E.; Kim, J.; Tusseau-Nenez, S.; Goldner, P.; Malta, O.L.; Peretti, J.; Gacoin, T. Polarized  
352 Luminescence of Anisotropic LaPO<sub>4</sub>:Eu Nanocrystal Polymorphs. *Journal of the American Chemical Society*  
353 **2018**, *140*, 9512–9517. doi:10.1021/jacs.8b03983.
- 354 19. Shalav, A.; Richards, B.S.; Trupke, T.; Krämer, K.W.; Güdel, H.U. Application of NaYF<sub>4</sub>:Er<sup>3+</sup> up-converting  
355 phosphors for enhanced near-infrared silicon solar cell response. *Applied Physics Letters* **2005**, *86*, 013505.  
356 doi:10.1063/1.1844592.
- 357 20. Wen, S.; Zhou, J.; Zheng, K.; Bednarkiewicz, A.; Liu, X.; Jin, D. Advances in highly doped upconversion  
358 nanoparticles. *Nature communications* **2018**, *9*, 2415.
- 359 21. Balabhadra, S.; Debasu, M.L.; Brites, C.D.; Ferreira, R.A.; Carlos, L.D. Upconverting nanoparticles working  
360 as primary thermometers in different media. *The Journal of Physical Chemistry C* **2017**, *121*, 13962–13968.
- 361 22. Zhou, J.; Liu, Q.; Feng, W.; Sun, Y.; Li, F. Upconversion luminescent materials: advances and applications.  
362 *Chemical reviews* **2014**, *115*, 395–465.
- 363 23. Wang, L.; Li, Y. Na (Y<sub>1</sub>.5Na<sub>0.5</sub>)F<sub>6</sub> single-crystal nanorods as multicolor luminescent materials. *Nano*  
364 *letters* **2006**, *6*, 1645–1649.
- 365 24. Wang, F.; Han, Y.; Lim, C.S.; Lu, Y.; Wang, J.; Xu, J.; Chen, H.; Zhang, C.; Hong, M.; Liu, X. Simultaneous  
366 phase and size control of upconversion nanocrystals through lanthanide doping. *nature* **2010**, *463*, 1061.
- 367 25. Gražulis, S.; Chateigner, D.; Downs, R.T.; Yokochi, A.F.T.; Quirós, M.; Lutterotti, L.; Manakova, E.; Butkus,  
368 J.; Moeck, P.; Le Bail, A. Crystallography Open Database – an open-access collection of crystal structures.  
369 *Journal of Applied Crystallography* **2009**, *42*, 726–729. doi:10.1107/S0021889809016690.
- 370 26. Grzechnik, A.; Bouvier, P.; Mezouar, M.; Mathews, M.D.; Tyagi, A.K.; Köhler, J. Hexagonal Na<sub>1.5</sub>Y<sub>1.5</sub>F<sub>6</sub> at  
371 High Pressures. *Journal of Solid State Chemistry* **2002**, *165*, 159–164. doi:10.1006/jssc.2001.9525.
- 372 27. Roy, D.M.; Roy, R. Controlled Massively Defective Crystalline Solutions with the Fluorite Structure. *Journal*  
373 *of The Electrochemical Society* **1964**, *111*, 421–429. doi:10.1149/1.2426145.
- 374 28. Górriller-Walrand, C.; Binnemans, K. Chapter 155 Rationalization of crystal-field parametrization; Elsevier,  
375 1996; Vol. 23, pp. 121–283.
- 376 29. Rodríguez-Carvajal, J. Recent advances in magnetic structure determination by neutron powder diffraction.  
377 *Physica B: Condensed Matter* **1993**, *192*, 55–69. doi:10.1016/0921-4526(93)90108-I.
- 378 30. Rodríguez-Carvajal, J. Recent developments of the program FULLPROF. *Commission on powder diffraction*  
379 *(IUCr). Newsletter* **2001**, *26*, 12–19.
- 380 31. Thompson, P.; Cox, D.E.; Hastings, J.B. Rietveld refinement of Debye–Scherrer synchrotron X-ray data  
381 from Al<sub>2</sub>O<sub>3</sub>. *Journal of Applied Crystallography* **1987**, *20*, 79–83. doi:10.1107/S0021889887087090.
- 382 32. Langford, J.I. A rapid method for analysing the breadths of diffraction and spectral lines using the Voigt  
383 function. *Journal of Applied Crystallography* **1978**, *11*, 10–14. doi:10.1107/S0021889878012601.
- 384 33. Langford, J.I.; Wilson, A.J.C. Scherrer after sixty years: A survey and some new results in the determination  
385 of crystallite size. *Journal of Applied Crystallography* **1978**, *11*, 102–113. doi:10.1107/S0021889878012844.
- 386 34. Guinier, A. *X-ray Diffraction in Crystals, Imperfect Crystals, and Amorphous Bodies*; Courier Corporation, 1994.
- 387 35. de Keijser, T.H.; Langford, J.I.; Mittemeijer, E.J.; Vogels, A.B.P. Use of the Voigt function in a single-line  
388 method for the analysis of X-ray diffraction line broadening. *Journal of Applied Crystallography* **1982**,  
389 *15*, 308–314. doi:10.1107/S0021889882012035.
- 390 36. Williamson, G.K.; Hall, W.H. X-ray line broadening from fcc aluminium and wolfram. *Acta Metallurgica*  
391 **1953**, *1*, 22–31. doi:10.1016/0001-6160(53)90006-6.
- 392 37. Halder, N.C.; Wagner, C.N.J. Analysis of the Broadening of Powder Pattern Peaks Using Variance, Integral  
393 Breadth, and Fourier Coefficients of the Line Profile. In *Advances in X-Ray Analysis*; Springer, Boston, MA,  
394 1966; pp. 91–102.
- 395 38. Halder, N.C.; Wagner, C.N.J. Separation of particle size and lattice strain in integral breadth measurements.  
396 *Acta Crystallographica* **1966**, *20*, 312–313. doi:10.1107/S0365110X66000628.